Article

Imaging tunable quantum Hall broken-symmetry orders in graphene

Alexis Coissard[1,5], David Wander[1,5], Hadrien Vignaud[1], Adolfo G. Grushin[1], Cécile Repellin[2], Kenji Watanabe[3], Takashi Taniguchi[4], Frédéric Gay[1], Clemens B. Winkelmann[1], Hervé Courtois[1], Hermann Sellier[1] & Benjamin Sacépé[1✉]

When electrons populate a flat band their kinetic energy becomes negligible, forcing them to organize in exotic many-body states to minimize their Coulomb energy[1–5]. The zeroth Landau level of graphene under a magnetic field is a particularly interesting strongly interacting flat band because interelectron interactions are predicted to induce a rich variety of broken-symmetry states with distinct topological and lattice-scale orders[6–11]. Evidence for these states stems mostly from indirect transport experiments that suggest that broken-symmetry states are tunable by boosting the Zeeman energy[12] or by dielectric screening of the Coulomb interaction[13]. However, confirming the existence of these ground states requires a direct visualization of their lattice-scale orders[14]. Here we image three distinct broken-symmetry phases in graphene using scanning tunnelling spectroscopy. We explore the phase diagram by tuning the screening of the Coulomb interaction by a low- or high-dielectric-constant environment, and with a magnetic field. In the unscreened case, we find a Kekulé bond order, consistent with observations of an insulating state undergoing a magnetic-field driven Kosterlitz–Thouless transition[15,16]. Under dielectric screening, a sublattice-unpolarized ground state[13] emerges at low magnetic fields, and transits to a charge-density-wave order with partial sublattice polarization at higher magnetic fields. The Kekulé and charge-density-wave orders furthermore coexist with additional, secondary lattice-scale orders that enrich the phase diagram beyond current theory predictions[6–10]. This screening-induced tunability of broken-symmetry orders may prove valuable to uncover correlated phases of matter in other quantum materials.

Narrow electronic energy bands provide an opportunity to explore many-body quantum phases of matter. The vanishingly small kinetic energy in these narrow bands leaves electrons subjected to interaction effects alone, resulting in the emergence of a wealth of correlated, topological and broken-symmetry phases[1–5]. Nearly perfect flat bands naturally develop in two-dimensional electron systems under a perpendicular magnetic field, B, as macroscopically degenerate Landau levels. There, the main consequence of Coulomb interaction is to generate incompressible—gapped—phases at half-integer filling of Landau levels, by favouring a spin-polarized ground state, a phenomenon called quantum Hall ferromagnetism[17].

In graphene, the additional valley degeneracy enriches the quantum Hall ferromagnetism with broken-symmetry states at every quarter filling[6,11]. A central challenge is to unveil the nature of the ground state of the gapped zeroth Landau level (zLL) at charge neutrality. Theory predicts a rich phase diagram of broken-symmetry states with different topological properties[7–10,18]. Although all are SU(4) ferromagnets, their exact spin and valley polarization (Fig. 1c) depends on a delicate balance between Zeeman energy and valley-anisotropy terms emerging from the lattice-scale interactions. Furthermore, the zLL wavefunctions feature a simple structure in which each valley degree of freedom is locked to one of the graphene's sublattices. This property isolates four possible broken-symmetry states with distinct sublattice or spin orders: a valley-polarized charge-density wave (CDW), a valley-polarized Kekulé bond (KB) order, a canted antiferromagnet (CAF) and a spin-polarized ferromagnet (F). Among them, the F order is a quantum Hall topological insulator harbouring conducting helical edge states, whereas the others are insulators with gapped edge states[19].

Experimentally, the main insights to distinguish different broken-symmetry states come from transport measurements. High-mobility graphene typically shows an unequivocal insulating behaviour at charge neutrality on increasing the perpendicular magnetic field[11,15,16,20,21]. However, a strong in-plane magnetic field that boosts the Zeeman effect and the ensuing spin polarization can induce a transition to the helical phase with F order[12]. An alternative strategy utilized a

[1]Université Grenoble Alpes, CNRS, Grenoble INP, Institut Néel, Grenoble, France. [2]Université Grenoble-Alpes, CNRS, LPMMC, Grenoble, France. [3]Research Center for Functional Materials, National Institute for Materials Science, Tsukuba, Japan. [4]International Center for Materials Nanoarchitectonics, National Institute for Materials Science, Tsukuba, Japan. [5]These authors contributed equally: Alexis Coissard, David Wander. ✉e-mail: benjamin.sacepe@neel.cnrs.fr
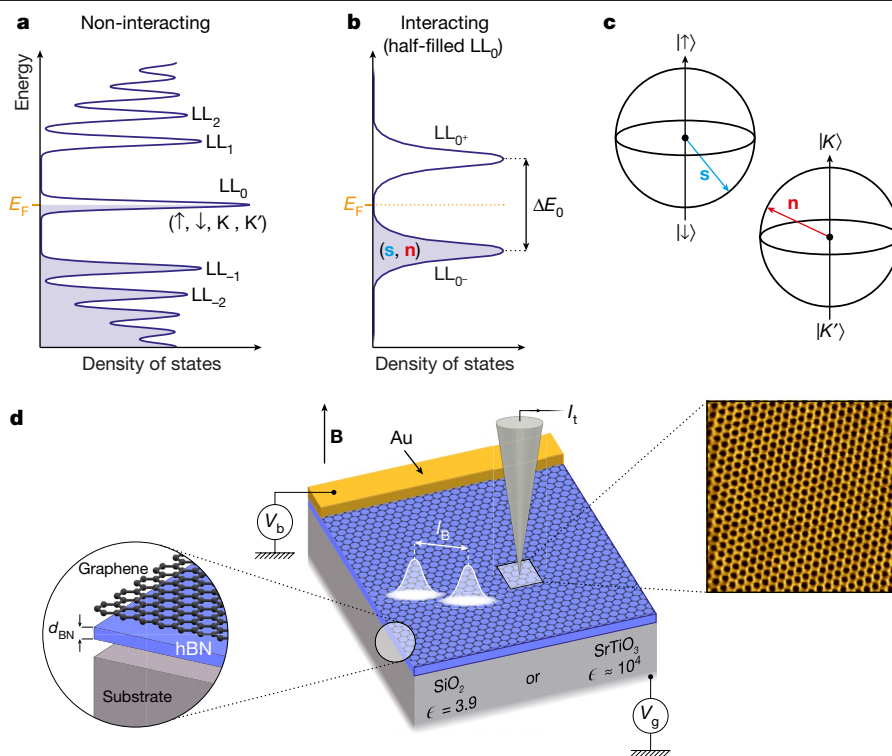
Fig. 1 | Landau level tunnelling spectroscopy in graphene. a, The non-interacting density of states of graphene under a perpendicular magnetic field. Each Landau level (LL_N, where N is the Landau level index) is spin ($\uparrow$, $\downarrow$) and valley (K, K′) degenerate, and emerges as a peak separated from others by cyclotron gaps. **b**, Owing to exchange interaction, the half-filled LL_0 at charge neutrality splits into two peaks $LL_{0\pm}$, thus opening an interaction-induced gap ΔE^0. The resulting broken-symmetry state features an SU(4) polarization with a spin polarization **s** and a valley polarization **n** evolving in the SU(4) Bloch sphere constructed on the spin and valley subspaces. **c**, Schematics of the individual Bloch spheres of the spin and valley subspaces. **d**, Schematics of the graphene samples. The two different substrates used are either SiO₂

(unscreened configuration) or the high-dielectric-constant SrTiO₃ (screened configuration). In both cases, graphene is biased with the voltage V_b through an ohmic contact (in yellow) and its charge carrier density is tuned by the voltage V_g applied to a back-gate electrode. The tunnelling current I_t is measured from the metallic tip. The tunnelling spectroscopy is performed under perpendicular magnetic field B. The white disks on the sample illustrate the Gaussian electronic wavefunction of LL_0 that extends on the scale of the magnetic length l_B. The left inset shows the graphene/hBN/substrate heterostructure, where d_{BN} is the hBN thickness. The right inset shows a 5×5 nm² STM image of the graphene honeycomb lattice measured on sample STO07 at 4 K and at 0 T.

high-dielectric-constant substrate to screen the long-range part of the Coulomb interaction[13]. This enables the helical phase to emerge at moderate perpendicular magnetic fields, which eventually transits to a weak insulator on increasing the magnetic field. Furthermore, a KB order has been observed recently in graphene on graphite, which, however, cannot be assessed by transport experiments owing to the conductive graphite layer[14]. These observations suggest that a broad part of the phase diagram can be explored.

Here we unambiguously identify three broken-symmetry states in the zLL of graphene by directly visualizing their lattice-scale order with scanning tunnelling microscopy (STM) and spectroscopy[22]. To access the different broken-symmetry states, we used two different dielectric materials as substrate, both equipped with a back-gate electrode: the standard silicon oxide (SiO₂) and the quantum paraelectric strontium titanium oxide (SrTiO₃) with a remarkably high static dielectric constant $\epsilon_{STO} \approx 10^4$ at low temperatures (Extended Data Fig. 1b). We fabricated samples consisting of monolayer graphene resting atop a thin hexagonal boron nitride (hBN) flake, deposited on the chosen substrate. To enable screening of the long-range Coulomb interaction[13], we selected hBN flakes (Extended Data Table 1) with thickness less than or of the order of the magnetic length $l_B = \sqrt{\hbar/eB}$ (where $\hbar$ is the reduced Planck constant and e is the electron charge) at low magnetic field, that is, the interelectron distance in the zLL. Figure 1d shows a schematic of the sample structure, where a metallic contact on the graphene serves to apply a voltage bias, V_b. All measurements were performed at 4.2 K.

Coulomb interaction screening

The Coulomb interaction strength can be readily assessed by tunnelling spectroscopy of the exchange gap that opens at half filling of the zLL[14] (Fig. 1a, b). Figure 2b shows a representative local tunnelling conductance spectrum, dI_t/dV_b versus V_b (where I_t is the tunnelling current), measured on sample STO07 under a perpendicular magnetic field of 14 T. In this measurement, the Fermi level is adjusted at charge neutrality, that is, at half filling of the zLL, by applying a back-gate voltage $V_g = 13$ V. Although all Landau levels with index $|N| \geq 1$ appear in the tunnelling conductance as sharp peaks separated by the cyclotron gap scaling as $\sqrt{|N|B}$ (Supplementary Information), the zLL splits into two peaks revealing the Coulomb gap ΔE^0, of the $\nu = 0$ broken-symmetry state (where ν is the Landau level filling factor), akin to earlier experiments in gallium arsenide[23]. For accurate measurements of the gap, which reaches its maximum value at half-filling[17], we measured the back-gate dependence of the tunnelling conductance as shown in Fig. 2a. The Landau level peaks form a staircase pattern, indicating the successive pinning of the Fermi level within each highly degenerate Landau level[24,25]. The absence of Coulomb diamond features seen in previous studies indicates that our measurements are not affected by a tip-induced quantum dot[26]. Analysis of individual spectra around charge neutrality enables us to evaluate ΔE^0, defined as the maximum separation between split peaks (red arrow in Fig. 2c, d). It is noted that tip-induced gating yields a negligible variation of filling factors of the order of 0.1 at the bias voltage of the split peaks (Supplementary Information).
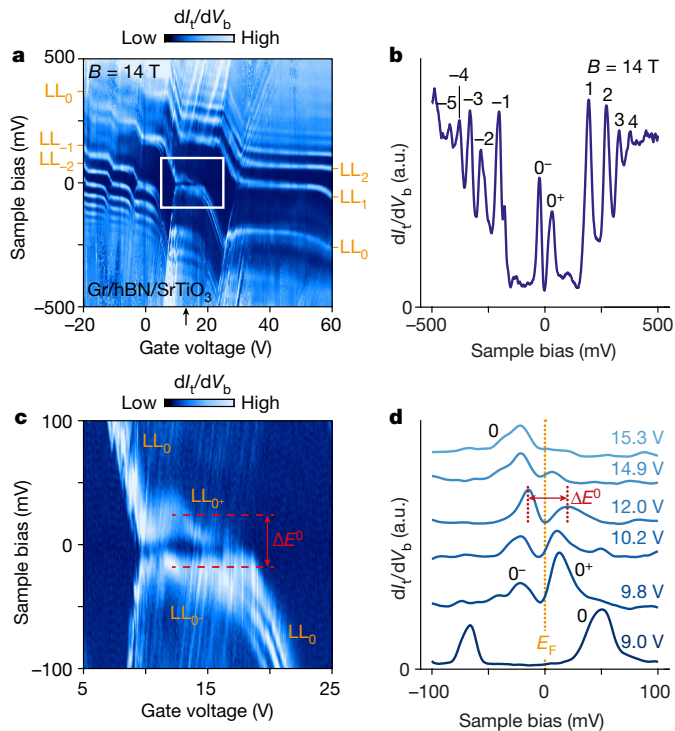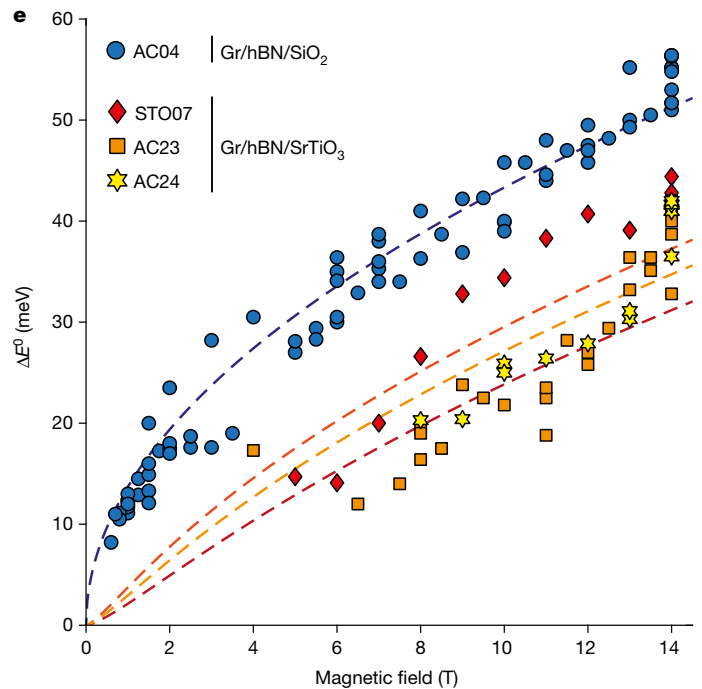
Fig. 2 | Quantum Hall ferromagnetic gap at charge neutrality. a, Local tunnelling conductance gate map measured on graphene (Gr) sample STO07 (SrTiO$_3$ substrate) at B = 14 T. The staircase pattern shows the successive pinning of the Fermi level E_F inside Landau levels. **b**, Tunnelling spectrum measured on the same sample at B = 14 T and V_g = 13 V, which corresponds to charge neutrality as indicated by the black arrow in **a**. With E_F at half filling, the zLL splits into two peaks LL$_{0\pm}$ that define the gap ΔE^0 of the broken-symmetry state. **c**, Zoom of the white rectangle in **a** showing the splitting of the LL$_0$. **d**, Spectra extracted from **c** at the back-gate voltages indicated on the right of

each curve. **e**, Evolution of ΔE^0 as a function of magnetic field for the four studied samples. For sample AC04 (SiO$_2$ substrate), the gap is fitted by the Coulomb energy $1/2\sqrt{\pi/2}\ \mathcal{E}_C \propto \sqrt{B}$, shown as a dashed blue line. For the three samples with SrTiO$_3$ substrates, ΔE^0 is decreased compared with sample AC04 owing to the substrate screening of the Coulomb interaction. The red, orange and yellow dashed lines correspond to the substrate-screened Coulomb energy $1/2\sqrt{\pi/2}\ \widetilde{\mathcal{E}}_C$, calculated with the respective hBN thickness of the samples.

Inspecting a systematic set of conductance maps for different magnetic field values, measured at various locations on the graphene surface, and on four different samples including SiO$_2$ and SrTiO$_3$ substrates (Extended Data Table 1), provides a robust determination of the B dependence of the energy gap. Figure 2e shows the resulting values of ΔE^0 as a function of the magnetic field.

We first focus on the unscreened case of sample AC04 (SiO$_2$ substrate) with the blue data points in Fig. 2e. A clear $\sqrt{B}$ dependence highlighted by the blue dashed line is observed starting at fields as low as 0.6 T and up to 14 T. This dependence reflects the growth of the Coulomb energy with B that scales as $\mathcal{E}_C = e^2/4\pi\epsilon_0\epsilon_r l_B \propto \sqrt{B}$, where ϵ_0 and ϵ_r are the vacuum permittivity and the relative permittivity surrounding the graphene, respectively. As the top graphene surface is exposed to vacuum, $\epsilon_r = (\epsilon_{BN} + 1)/2 \approx 2.3$, where $\epsilon_{BN} \approx 3.6$ is the hBN relative permittivity. Theoretically, ΔE^0 is expected to be $1/2\sqrt{\pi/2}\ \mathcal{E}_C$ (ref. [17]). We plot this quantity in Fig. 2e (blue dashed curve) by adjusting ϵ_r to 2.6, which is consistent with the expected value for the relative permittivity. Such a quantitative agreement demonstrates the significance of our spectroscopy to assess the interaction-induced gap.

Remarkably, turning to the screened case with the SrTiO$_3$ substrate yields gap values conspicuously smaller than those obtained on the sample on SiO$_2$ (see red, orange and yellow data points in Fig. 2e). This demonstrates a clear screening of the Coulomb interaction by the high dielectric constant of the substrate. Electrostatic considerations that account for the thin hBN bottom layer lead to a substrate-screened Coulomb energy scale $\widetilde{\mathcal{E}}_C = \mathcal{E}_C \times S(B)$ that is mitigated by a screening factor $S(B) \approx 1 - \frac{\epsilon_{STO} - \epsilon_r}{\epsilon_{STO} + \epsilon_r} \frac{l_B}{\sqrt{l_B^2 + 4d_{BN}^2}}$, where d_{BN} is the hBN thickness[13].

Consequently, electrons in graphene are subjected to an unusual B-dependent screening that depends on the ratio l_B/d_{BN} and is most efficient at low magnetic fields. In Fig. 2e, the red, orange and yellow dashed curves show $\widetilde{\mathcal{E}}_C$ calculated with the hBN thickness of the respective samples. Although the use of $\widetilde{\mathcal{E}}_C$ is strictly valid only for hBN-encapsulated graphene, we obtain a decent agreement with our data, despite some scattering for sample STO07.

Tunable lattice-scale orders

We now turn to the central result of this work, benchmarking the lattice-scale orders of the charge-neutral broken-symmetry state, upon tuning the screening of the Coulomb interaction. Figure 3 shows three STM images taken at the energy of a split zLL peak, on the SiO$_2$ sample AC04 at B = 14 T (Fig. 3d), and on the SrTiO$_3$ sample AC23 at B = 14 T (Fig. 3e) and B = 4 T (Fig. 3f). These panels thus cover three regimes for Coulomb interaction that we qualify as unscreened, moderately screened and screened, respectively. For the unscreened case in Fig. 3d, we observe a Kekulé distortion bond-order pattern of the electronic wavefunction, consistent with an independent recent study[27], indicating that spin-singlet pairs of electrons are localized on one bond out of three per carbon atom of the graphene honeycomb lattice. This order is stable down to B = 3 T (Fig. 4e). With the SrTiO$_3$ substrates at high magnetic field, that is, under moderate screening, another lattice-scale order develops with a stark valley polarization: the CDW ground-state with the spin-singlet pairs now mostly localized on a single sublattice (Fig. 3e). This CDW order is found to be independent of the presence of a moiré superlattice formed with the hBN layer (Extended Data Figs. 8b, 9b). Finally, at low magnetic field (4 T in Fig. 3f), this CDW
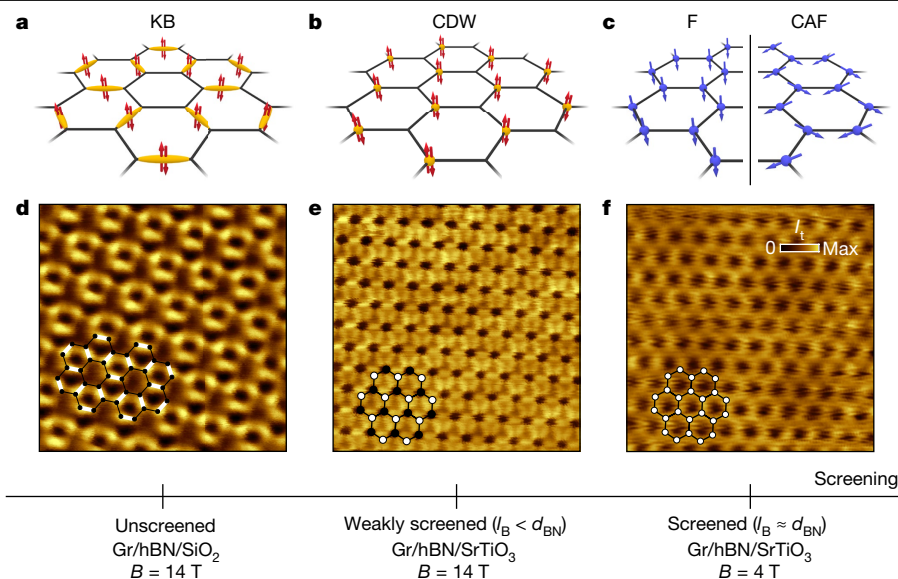
Fig. 3 | Tunable broken-symmetry states of charge-neutral graphene.
a–**c**, Lattice-scale order drawings of the four possible broken-symmetry states in charge-neutral graphene under a perpendicular magnetic field. **a**, The KB order. **b**, The CDW with sublattice polarization. **c**, The spin-polarized F and CAF ground states. **d**–**f**, Three 2.6×2.6 nm^2 STM images taken in constant height mode. **d**, STM image on sample AC04 (unscreened graphene) at $B = 14$ T and $V_b = 25$ mV, which unveils a KB order. **e**, At $B = 14$ T (weakly screened graphene,

$l_B = 7$ nm $< d_{BN} = 12$ nm) and $V_b = 40$ mV, the sample AC23 shows a sublattice CDW. **f**, At $B = 4$ T (screened graphene, $l_B = 13$ nm $\approx d_{BN} = 12$ nm) and $V_b = 20$ mV, we find a valley-unpolarized phase consistent with the spin-polarized helical phase. For each image, we superposed a corresponding lattice drawing emphasizing the bond order, the sublattice polarization and the honeycomb lattice, respectively. The black horizontal arrow indicates the strength of substrate screening.

order disappears, revealing a valley-unpolarized graphene honeycomb lattice, which points to a spin order, that is, the F or CAF orders.

Kekulé bond order

Going further, we show that additional fine structures emerge at the lattice scale, enriching the predicted phase diagram. The KB order

features an unexpected, faint CDW that has the periodicity of the Kekulé unit cell. This coexisting order is readily seen in Fig. 4a: a nicely formed Kekulé pattern shows an enhanced local wavefunction amplitude inside one hexagon of the honeycomb that repeats periodically on the Kekulé triangular lattice, as indicated by the blue circles and dashed lines in Fig. 4b. Figure 4c provides a representation of the latter superimposed on the honeycomb and Kekulé lattices. This CDW, which we label as
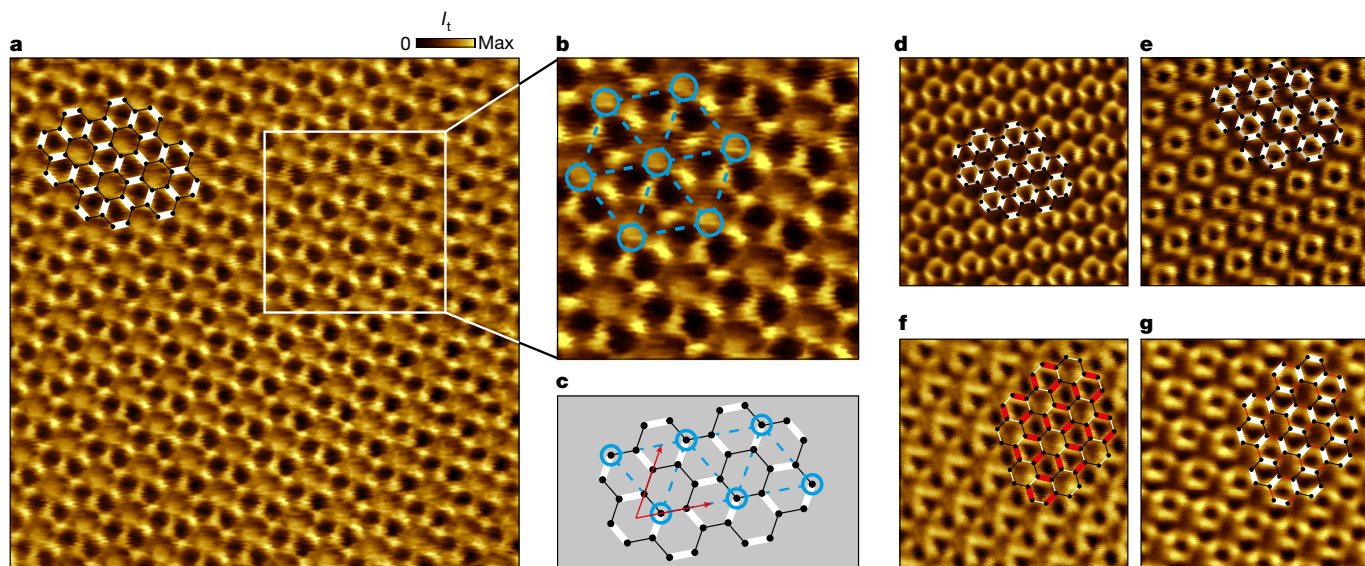
Fig. 4 | KB order in unscreened charge-neutral graphene. a, A 5×5 nm^2 STM image on sample AC04, at $B = 14$ T and $V_b = 25$ mV. The KB lattice, where both electrons of the broken-symmetry state are localized on one C–C bond out of three, is shown in overlay with the stronger bonds highlighted in thick white. **b**, A zoom of **a**, where we observe a secondary CDW order featuring a triangular lattice (drawn in blue) with a parameter matching the one of the Kekulé lattice ($\sqrt{3}$ times the graphene lattice parameter). **c**, The structure of the KB lattice, where the basis vectors of the KB order lattice are indicated in red. **d**, **e**, Two

3×3 nm^2 images showing asymmetric Kekulé patterns. **d**, At $B = 14$ T and $V_b = 2$ mV, the three Kekulé strong bonds are partially merged. **e**, At $B = 3$ T and $V_b = 30$ mV, three Kekulé strong bonds are completely merged and form a circle-like pattern. **f**, **g**, Two 3×3 nm^2 images at $B = 14$ T and $V_b = 25$ meV acquired at the same position a few minutes apart, showing the transition between two degenerate Kekulé configurations from the red Kekulé lattice in **f**, to the white one in **g**. Both lattices in overlay are at the same position.
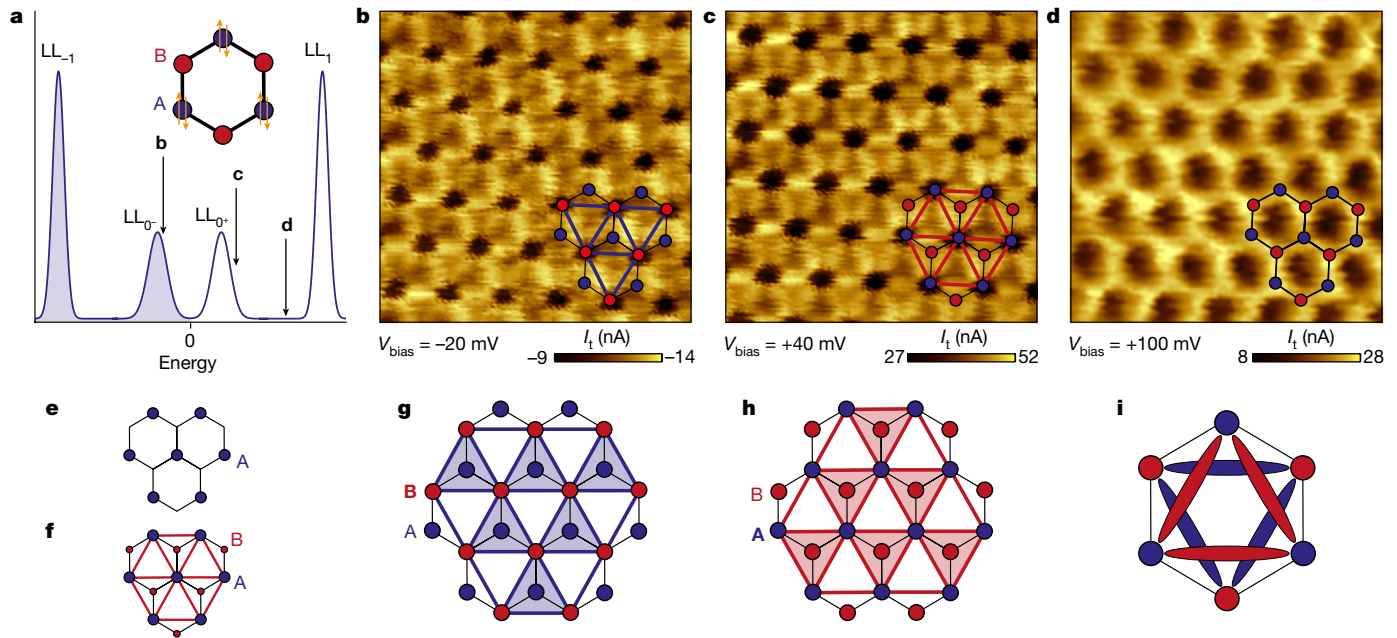
Fig. 5 | CDW order in moderately screened charge-neutral graphene.
a, Simulated Landau spectrum indicating the bias voltage positions of the subsequent 1.5×1.5 nm^2 constant-height STM images, all acquired at $B = 14$ T and at the same location on sample AC23. Inset: convention for the CDW lattice. The blue sublattice A is doubly occupied whereas the red sublattice B is empty. **b**, Image at $V_b = -20$ mV with the CDW lattice in overlay: the sublattice B (empty) appears as dark spots at negative bias and intra-sublattice bonds are visible as bright lines between them. **c**, Similarly, at the positive bias of $V_b = +40$ mV, the sublattice A (doubly occupied) appears as dark spots and intra-sublattice bonds are visible as bright lines between them. It is noted that the colour scale

in **b** is inverted with respect to that in **c**, as the tunnelling current is negative due to the negative bias. **d**, At $V_b = 100$ mV, the CDW is no longer visible and the honeycomb lattice appears instead. **e**, A CDW with full sublattice polarization, as predicted in ref. [10], compared with a CDW with partial sublattice polarization in **f**. The symmetry-allowed triangular bond order is suppressed in **e**, and coexists with the CDW in **f**, where a triangular lattice emerges owing to a symmetry-allowed sublattice hopping asymmetry. In **f**, the difference in size for the A and B atoms represents the partial sublattice polarization. **g**, **h**, Sketches showing the CDW sublattice inversion between negative bias (**g**) and positive bias (**h**). **i**, Structure of the intra-sublattice bonds.

K-CDW, is different from the CDW broken-symmetry state as it shows a triangular lattice with a parameter $\sqrt{3}$-times larger than the graphene lattice parameter. The tripled unit cell of the K-CDW is reminiscent of CDW phases observed to compete with the Kekulé order in extended Hubbard models[28,29] at $B = 0$, but have not been reported or predicted at finite B. We also observed other situations in which this K-CDW induces a pronounced asymmetry of the Kekulé pattern, with a more or less merging of the Kekulé strong bonds (Extended Data Figs. 2, 3). This is illustrated by the evolution from the mostly symmetric Kekulé lattice shown in Fig. 4a to the asymmetric Kekulé lattices shown in Fig. 4d, e. If on some images the strong bonds are still visible (Fig. 4d), they can also merge with each other, forming a circle-like pattern seen in Fig. 4e.

Interestingly, both the KB order and K-CDW vary with time. For instance, Fig. 4f, g shows a spontaneous transition from one of the three possible degenerate Kekulé lattices to another, while continuously imaging the same location. Similar changes for the K-CDW are shown in Extended Data Figs. 4, 5.

CDW order

In screened graphene, likewise, close inspection of the CDW broken-symmetry state reveals striking fine structures. Here we assume that the electron doublets of the CDW are localized on the sublattice A (in blue), whereas the sublattice B is empty (in red), as in the inset of Fig. 5a. We start by deciphering Fig. 5b, c, taken at the same location, and comparing the occupied and empty orbitals of the same atoms. In both images, the CDW appears as dark spots featuring a triangular symmetry and corresponding to the atoms of a single sublattice (the sublattice B in Fig. 5b and the sublattice A in Fig. 5c), whereas atoms of the other sublattice are not visible. Extracting electrons from the occupied states into the STM tip at negative sample bias leads to a

low tunnelling current on the empty atoms of the sublattice B (dark spots in Fig. 5b). Similarly, injecting electrons from the STM tip into the empty states at positive sample bias leads to a low current on the already doubly occupied atoms of the sublattice A (dark spots in Fig. 5c).

In addition, inspecting Fig. 5c, we see that atoms of sublattice B (red spots in the inset) are located in the middle of a triangular lattice formed by bright lines joining the doubly occupied atoms of the sublattice A, which correspond to a high density of empty states. One can also notice in Fig. 5c that the triangular cells that contain atoms B are brighter than the other empty cells, which is consistent with the enhancement of the local density of empty states by the B atoms. We illustrate this unusual sublattice inversion with the lattice drawings in Fig. 5g, h, where the density of occupied and empty states are colour-coded blue and red, respectively. Figure 5i summarizes this remarkable inverted pattern by superposing the empty (red) and occupied (blue) states on the same carbon hexagon.

This additional triangular order that accompanies the CDW in Fig. 5 was not expected by theory[10]. Such a sublattice bond asymmetry, $t_{2,A} \neq t_{2,B}$ (where, $t_{2,A}$ and $t_{2,B}$ are the second-nearest-neighbour bond expectation values of sublattices A and B, respectively), is generically permitted in the CDW phase as it gaps out the zLL with the same matrix structure as a sublattice charge imbalance[30] (Methods and Extended Data Figs. 6, 7). It becomes visible when the sublattice degree of freedom is partially polarized (Fig. 5e, f). We conjecture that this partial sublattice polarization could originate from Landau level mixing, as the sublattice index is decoupled from the valley index in higher Landau levels[31–33].

Implications for transport experiments

The observation of these three ground states has profound implications for the understanding of transport properties at charge neutrality. For

Article

the unscreened case, corresponding to virtually all transport experiments, the KB order contradicts the transition scenario from the conjectured CAF phase to the helical F phase tuned by the Zeeman field[10,12], as well as recent magnon transmission experiments[34–37] that imply magnetism. Nonetheless, a recent prediction[33] suggests that both KB order and CAF phases could coexist, thus accounting for the experimental dissonance. Our observation of a subdominant K-CDW order adds yet another flavour to the phase diagram, which was not anticipated thus far and deserves further theoretical attention. Similarly, the nature of edge excitations may be more complex than initially thought[38]. A definitive conclusion on the existence of an underlying magnetism in this ground state and its possible spin texture at the lattice scale (Fig. 3c) would require further spin-filtered scanning tunnelling experiments.

Furthermore, our observation of coexisting orders implies that the nature of bulk excitations in this insulating phase must be revisited[39]. The time-varying nature of the KB order and K-CDW, indicating some depinning mechanisms and the presence of domain walls, may contribute to charge transport, in parallel to skyrmion excitations. A Kosterlitz–Thouless phase transition driven by topological Kekulé-vortex zero modes[40] has been predicted[41] and discussed experimentally[15,16].

In the screened case, we observed the CDW persisting from $B = 14$ T to $B = 7$ T (Extended Data Fig. 8) and disappearing at $B = 4$ T in favour of a valley-unpolarized phase at lower magnetic field. This phase transition is consistent with the spin-polarized helical phase observed in transport measurements[13], which is replaced by a weakly insulating phase at high fields, corresponding to the CDW phase found in this work. The scenario explaining the change of ground state owing to substrate screening was accounted for by a modification of renormalization effects of the valley-anisotropy energies by the (screened) long-range Coulomb interaction[13]. Although it is difficult to assess this renormalization experimentally, the substrate screening of the Coulomb interaction evidenced by our spectroscopy of the zLL gap indicates that such a mechanism is likely to be at play. As the screening exhibits an inversely proportional B dependence, our findings, supported by transport experiments, confirm a modification of the valley-anisotropy energies on varying the magnetic field in this specific substrate-screened configuration.

Ultimately, at much higher fields such that $l_B \ll d_{BN}$, one should expect in graphene samples on $SrTiO_3$ another transition from the CDW to the KB phase. In this situation, the substrate screening vanishes and the Coulomb energy scale asymptotically reaches its bare value.

Online content

Any methods, additional references, Nature Research reporting summaries, source data, extended data, supplementary information, acknowledgements, peer review information; details of author contributions and competing interests; and statements of data and code availability are available at https://doi.org/10.1038/s41586-022-04513-7.

1. Cao, Y. et al. Correlated insulator behaviour at half-filling in magic-angle graphene superlattices. *Nature* **556**, 80–84 (2018).
2. Cao, Y. et al. Unconventional superconductivity in magic-angle graphene superlattices. *Nature* **556**, 43–50 (2018).
3. Wong, D. et al. Cascade of electronic transitions in magic-angle twisted bilayer graphene. *Nature* **582**, 198–202 (2020).
4. Zondiner, U. et al. Cascade of phase transitions and Dirac revivals in magic-angle graphene. *Nature* **582**, 203–208 (2020).
5. Saito, Y. et al. Hofstadter subband ferromagnetism and symmetry-broken Chern insulators in twisted bilayer graphene. *Nat. Phys.* **17**, 478–781 (2021).
6. Nomura, K. & MacDonald, A. H. Quantum Hall ferromagnetism in graphene. *Phys. Rev. Lett.* **96**, 256602 (2006).
7. Alicea, J. & Fisher, M. P. A. Graphene integer quantum Hall effect in the ferromagnetic and paramagnetic regimes. *Phys. Rev. B* **74**, 075422 (2006).
8. Herbut, I. F. Theory of integer quantum Hall effect in graphene. *Phys. Rev. B* **75**, 165411 (2007).
9. Jung, J. & MacDonald, A. H. Theory of the magnetic-field-induced insulator in neutral graphene sheets. *Phys. Rev. B* **80**, 235417 (2009).
10. Kharitonov, M. Phase diagram for the $v = 0$ quantum Hall state in monolayer graphene. *Phys. Rev. B* **85**, 155439 (2012).
11. Young, A. F. et al. Spin and valley quantum Hall ferromagnetism in graphene. *Nat. Phys.* **8**, 550–556 (2012).
12. Young, A. F. et al. Tunable symmetry breaking and helical edge transport in a graphene quantum spin Hall state. *Nature* **505**, 528–532 (2014).
13. Veyrat, L. et al. Helical quantum Hall phase in graphene on $SrTiO_3$. *Science* **367**, 781–786 (2020).
14. Li, S.-Y., Zhang, Y., Yin, L.-J. & He, L. Scanning tunneling microscope study of quantum Hall isospin ferromagnetic states in the zero Landau level in a graphene monolayer. *Phys. Rev. B* **100**, 085437 (2019).
15. Checkelsky, J. G., Li, L. & Ong, N. P. Zero-energy state in graphene in a high magnetic field. *Phys. Rev. Lett.* **100**, 206801 (2008).
16. Checkelsky, J. G., Li, L. & Ong, N. P. Divergent resistance at the Dirac point in graphene: evidence for a transition in a high magnetic field. *Phys. Rev. B* **79**, 115434 (2009).
17. Ezawa, Z. F. Quantum Hall Effects (World Scientific, 2013).
18. Herbut, I. F. SO(3) symmetry between Néel and ferromagnetic order parameters for graphene in a magnetic field. *Phys. Rev. B* **76**, 085432 (2007).
19. Kharitonov, M., Juergens, S. & Trauzettel, B. Interplay of topology and interactions in quantum Hall topological insulators: U(1) symmetry, tunable Luttinger liquid, and interaction-induced phase transitions. *Phys. Rev. B* **94**, 035146 (2016).
20. Zhang, Y. et al. Landau-level splitting in graphene in high magnetic fields. *Phys. Rev. Lett.* **96**, 136806 (2006).
21. Abanin, D. A. et al. Dissipative quantum Hall effect in graphene near the Dirac point. *Phys. Rev. Lett.* **98**, 196806 (2007).
22. Andrei, E. Y., Li, G. & Du, X. Electronic properties of graphene: a perspective from scanning tunneling microscopy and magnetotransport. *Rep. Prog. Phys.* **75**, 056501 (2012).
23. Dial, O. E., Ashoori, R. C., Pfeiffer, L. N. & West, K. W. High-resolution spectroscopy of two-dimensional electron systems. *Nature* **448**, 176–179 (2007).
24. Luican, A., Li, G. & Andrei, E. Y. Quantized Landau level spectrum and its density dependence in graphene. *Phys. Rev. B* **83**, 041405(R) (2011).
25. Chae, J. et al. Renormalization of the graphene dispersion velocity determined from scanning tunneling spectroscopy. *Phys. Rev. Lett.* **109**, 116802 (2012).
26. Jung, S. et al. Evolution of microscopic localization in graphene in a magnetic field from scattering resonances to quantum dots. *Nat. Phys.* **7**, 245–251 (2011).
27. Liu, X. et al. Visualizing broken symmetry and topological defects in a quantum Hall ferromagnet. *Science* **375**, 321–326 (2021).
28. Motruk, J., Grushin, A. G., de Juan, F. & Pollmann, F. Interaction-driven phases in the half-filled honeycomb lattice: an infinite density matrix renormalization group study. *Phys. Rev. B* **92**, 085147 (2015).
29. Capponi, S. & Läuchli, A. M. Phase diagram of interacting spinless fermions on the honeycomb lattice: a comprehensive exact diagonalization study. *Phys. Rev. B* **92**, 085146 (2015).
30. Alba, E., Fernandez-Gonzalvo, X., Mur-Petit, J., Pachos, J. K. & Garcia-Ripoll, J. J. Seeing topological order in time-of-flight measurements. *Phys. Rev. Lett.* **107**, 235301 (2011).
31. Peterson, M. R. & Nayak, C. Effects of Landau level mixing on the fractional quantum Hall effect in monolayer graphene. *Phys. Rev. Lett.* **113**, 086401 (2014).
32. Feshami, B. & Fertig, H. A. Hartree–Fock study of the $v = 0$ quantum Hall state of monolayer graphene with short-range interactions. *Phys. Rev. B* **94**, 245435 (2016).
33. Das, A., Kaul, R. K. & Murthy, G. Coexistence of canted antiferromagnetism and bond-order in $v = 0$ graphene. *Phys. Rev. Lett.* **128**, 106803 (2021).
34. Takei, S., Yacobi, A., Halperin, B. I. & Tserkovnyak, Y. Spin superfluidity in the $v = 0$ quantum Hall state of graphene. *Phys. Rev. Lett.* **116**, 216801 (2016).
35. Wei, D. S. et al. Electrical generation and detection of spin waves in a quantum Hall ferromagnet. *Science* **362**, 229–233 (2018).
36. Stepanov, P. et al. Long-distance spin transport through a graphene quantum Hall antiferromagnet. *Nat. Phys.* **14**, 907–911 (2018).
37. Assouline, A. et al. Unveiling excitonic properties of magnons in a quantum Hall ferromagnet. *Nat. Phys.* **17**, 1369–1374 (2021).
38. Knothe, A. & Jolicoeur, T. Edge structure of graphene monolayers in the $v = 0$ quantum Hall state. *Phys. Rev. B* **92**, 165110 (2015).
39. Atteia, J., Lian, Y. & Goerbig, M. O. Skyrmion zoo in graphene at charge neutrality in a strong magnetic field. *Phys. Rev. B* **103**, 035403 (2021).
40. Hou, C.-Y., Chamon, C. & Mudry, C. Electron fractionalization in two-dimensional graphene-like structures. *Phys. Rev. Lett.* **98**, 186809 (2007).
41. Nomura, K., Ryu, S. & Lee, D.-H. Field-induced Kosterlitz–Thouless transition in the $N = 0$ Landau level of graphene. *Phys. Rev. Lett.* **103**, 216801 (2009).

Methods

Sample fabrication

Graphene/hBN heterostructures were assembled from exfoliated flakes with the van der Waals pick-up technique using a polypropylene carbonate polymer[42]. Stacks were deposited using the methods described in ref. [43] (for sample STO07) or in ref. [44] (for samples AC04, AC23 and AC24), on either highly doped Si wafers with a 285-nm-thick SiO_2 layer, or 500-μm-thick $SrTiO_3$ [100] substrates cleaned with hydrofluoric acid buffer solution before deposition of the graphene/hBN heterostructures (a titanium/gold bilayer was deposited later on the other side of the $SrTiO_3$ substrate to enable the back-gate effect). The geometrical parameters of the samples are listed in Extended Data Table 1. Electron-beam lithography using a polymethyl methacrylate resist was used to pattern a guiding markerfield on the whole 5×5 mm^2 substrate to drive the STM tip towards the device. Chromium/gold electrodes contacting the graphene flake were also patterned by electron-beam lithography and metalized by e-gun evaporation. Samples were thermally annealed at 350 °C in vacuum under an halogen lamp to remove resist residues and clean graphene, before being mounted into the STM where they were heated in situ during the cooling to 4.2 K.

Measurements

Experiments were performed with a home-made hybrid STM and atomic force microscope (AFM) operating at a temperature of 4.2 K in magnetic fields up to 14 T. The AFM mode is used to guide the tip towards the graphene device. The sensor consists of a hand-cut platinum–iridium tip glued on the free prong of a tuning fork, the other prong being glued on a Macor plate. Once mounted inside the STM, the tip is roughly aligned over the sample at room temperature and then guided towards the graphene in AFM mode at low temperature using the guiding markerfield. Scanning tunnelling spectroscopy was performed using a lock-in amplifier technique with a modulation frequency of 263 Hz and a root-mean-square modulation voltage between 1 mV and 5 mV depending on the spectral range of interest. Imaging of the zLL lattice-scale orders was carried out in STM constant-height mode. Starting from a tunnelling contact at $V_b = 300$ mV and $I_t = 1$ nA with the Z-regulation on, we switch off the regulation and lower the bias voltage to either energies corresponding to the $LL_{0\pm}$ peaks, which drastically decreases the tunnelling current. We then manually approach the tip towards the graphene until the recovery of a tunnelling current of a few nanoamperes. STM images of the tunnelling current measured while scanning at a constant tip–sample distance subsequently yield atomically resolved images of the honeycomb lattice or lattice-scale orders.

Dielectric constant of SrTiO₃ in magnetic field

We show here how to estimate the $SrTiO_3$ dielectric constant, ϵ_{STO}, from tunnelling conductance gate maps. ϵ_{STO} is related to the global dielectric constant of the back gate, ϵ_r, which can be obtained by modelling the back-gate capacitance C_g as the sum of the series capacitances of $SrTiO_3$ and hBN assuming plane capacitors : $\frac{1}{C_g} = \frac{1}{C_{STO}} + \frac{1}{C_{BN}} \Rightarrow \frac{d_{STO} + d_{BN}}{\epsilon_r} = \frac{d_{STO}}{\epsilon_{STO}} + \frac{d_{BN}}{\epsilon_{BN}}$. As $d_{BN} \approx 10$ nm $\ll d_{STO} = 500$ μm, we write the gate dielectric constant as $\epsilon_r = \epsilon_{STO}\left(1 + \frac{d_{BN}}{d_{STO}}\frac{\epsilon_{STO}}{\epsilon_{BN}}\right)^{-1}$. Numerically, $\epsilon_{BN} \approx 3.6$ and $\epsilon_{STO} \approx 10^4$ at low temperature[45], so that $d_{BN}\epsilon_{STO}/d_{STO}\epsilon_{BN} \approx 0.1$. We can thus assume that $\epsilon_r \approx \epsilon_{STO}$.

To estimate ϵ_r as a function of the back-gate voltage, V_g, we consider the tunnelling conductance gate map of Fig. 2a (sample STO07) from which we can extract some values of the back-gate voltage at specific filling factors v. Note that the electron–hole asymmetry visible in this gate map stems from the nonlinear behaviour of ϵ_{STO} with gate voltage[13,46–48]. In Extended Data Fig. 1a, we plot the line cut of the gate map at zero bias, averaged on a range of ±20 meV around this value. We clearly observe the different non-zero conductance plateaus forming when the Fermi energy E_F is pinned inside one LL, with gaps in-between.

As the gate voltages at the middle of those gaps correspond to completely filled and empty LLs, we identify the positions in gate voltage of the integer filling factors $v = -10$, $v = -6$, $v = -2$ and $v = 2$. These values are converted into charge carrier density values n in Extended Data Fig. 1b using $v = n\phi_0/B$ with $\phi_0 = h/e$ the flux quantum and n the charge carrier density. A polynomial of degree five fits and interpolates the evolution of n with V_g. From this fit, charge neutrality point (CNP) at $n = 0$ is achieved at the back-gate voltage $V^{CNP} = 13.5$ V. We then straightforwardly obtain the V_g dependence of ϵ_r via $\epsilon_r = \frac{d_{STO}}{\epsilon_0}\frac{en}{V_g - V^{CNP}}$

The red curve in Extended Data Fig. 1b shows the resulting ϵ_r, which decreases with increasing gate voltage and ranges between 12,500 and 3,500. A similar $\epsilon_r(V_g)$ profile but with slightly weaker values is obtained for sample AC23 ($3,000 < \epsilon_r < 11,500$). Finally, using the fit of the filling factor v, we can rescale the gate map as a function of v as shown in Extended Data Fig. 1c. In particular, it is noted that in the rescaled map the interaction-induced gap is maximal at charge neutrality $v = 0$, as expected considering that the exchange interaction is maximal at half-filling of the zLL.

Asymmetry of the KB pattern

In Extended Data Fig. 2a, we show an STM image of an asymmetric KB pattern. Extended Data Fig. 2b shows the corresponding two-dimensional Fourier transform (2D-FT). The 2D-FT is mainly composed of three hexagons, defined by the yellow, red and blue encircled peaks. To decipher the 2D-FT, we filter the STM image by considering certain peaks only. The yellow peaks alone yield the usual honeycomb lattice in Extended Data Fig. 2c. The red peaks give the image shown in Extended Data Fig. 2d, which features a triangular lattice. When we superimpose the KB lattice drawing, we notice that each bright point of the triangular lattice in Extended Data Fig. 2d falls either on the strong white bonds of the Kekulé lattice or at the centre of the hexagons devoid of strong bond: the addition of both images yields the bond-density wave shown in Extended Data Fig. 2e where we have filtered the STM image by considering this time both yellow and red peaks and mostly recovered the original KB pattern. This also justifies why the hexagon devoid of strong bond in the KB pattern appears brighter than the neighbouring hexagons composed of three strong bonds, similarly visible in Fig. 4a. Note that the presence of two red peaks with halved amplitude in one direction is responsible of the slight asymmetry that is already visible in Extended Data Fig. 2e.

In Extended Data Fig. 2f, we show the image obtained after filtering using only the blue peaks. We observe a strongly asymmetric triangular lattice encoding the Kekulé spatial modulation at $\sqrt{3}$ times the graphene lattice parameter. The asymmetry arises from a large asymmetry between the blue peaks in the 2D-FT, where two peaks in one direction are twice as high as the others. This yields dissimilar weights to the bond-density wave, as shown in Extended Data Fig. 2g where we have filtered considering red and blue peaks, and explains the strong asymmetry we observe in the KB pattern, which is fully recovered in Extended Data Fig. 2h where we have filtered with the yellow, red and blue peaks. We conjecture that this strong asymmetry of the 2D-FT originates from the existence of the K-CDW order whose contribution is visible in Extended Data Fig. 2f, as in the symmetric KB pattern (where this K-CDW order is not visible) there is no such asymmetry between the blue and red peaks.

Bias dependence of the KB order

In Extended Data Fig. 3, we show constant-height-mode STM images where we have changed the sample bias V_b during scanning. The red and blue arrows on the right of each image show the direction of the slow-scan axis, and their colour corresponds to the actual sample bias, which is indicated in the bottom panels. In Extended Data Fig. 3a, we clearly observe a contrast inversion when switching the sample bias from LL_{0+} to LL_{0-}, with the continuity of the KB pattern at the interface. In Extended Data Fig. 3b, we see the transition from the usual honeycomb

lattice to the KB pattern when switching the sample bias from LL_1 to LL_{0+}. This indicates that both the KB order and the underlying K-CDW disappear when the bias voltage is away from the zLL peaks, which rules out a tip-induced artefact as the origin of the observed KB order.

K-CDW configuration change

We illustrate here the time-varying nature of the K-CDW. In Extended Data Fig. 4, we show three successive images acquired in a row at the same position and $V_b = 2$ mV. The vertical arrow on the left of each image indicates the direction of the slow-scan axis. Figure 4d belongs to the same set of image acquisition. In Extended Data Fig. 4a, the lattice in overlay describes the asymmetric KB pattern, with the white links being the strong bonds of the KB order, whereas the asymmetry that comes from the K-CDW order makes the hexagons with blue weak bonds brighter than the hexagons with red weak bonds. The next image in Extended Data Fig. 4b (duration of each image, 53 s) starts from the bottom, where we observe the same KB pattern. However, a jump occurs at the line indicated by the red arrows, and, after that, in the top part of the image, the asymmetry of the KB pattern is reversed. Using the lattice in overlay as a guide for the eye, we see that the red hexagons are brighter (owing to the three strong white bonds almost merging together), such that the new pattern is the mirror of the previous one. Eventually, the next image in Extended Data Fig. 4c shows this new pattern with brighter red hexagons on the whole area, and the next images we realized during several minutes happened to be identical. This indicates that the K-CDW order transited and reversed the asymmetry of the KB phase. It is noted that the pattern of the strong white bonds, which defines the KB order, stays unchanged in the three images (in opposition to the KB order transition shown in Fig. 4f, g).

The asymmetry reversal of the KB order owing to the K-CDW transition is well seen in the 2D-FT of both images in Extended Data Fig. 4a, c (top insets). For Extended Data Fig. 4a, the K-CDW appears in the inner hexagon, where the two peaks encircled in green are twice as bright as the other four peaks. On the contrary, for Extended Data Fig. 4c, it is now the yellow peaks that are brighter than the other four, with the amplitude of the green peaks lowered. The change of the direction of the two brighter peaks induces the change of the asymmetry pattern of the KB order. Interestingly, the outermost hexagon, which corresponds to the bond-density wave, also features a change in the intensity of its peaks: in Extended Data Fig. 4a, the blue peaks are halved in amplitude whereas in Extended Data Fig. 4c the red peaks are halved. This does not yield any notable change of the KB pattern but this may mean that the bond-density wave and the K-CDW are entangled.

Therefore, the asymmetry of the KB patterns we observed depends on the K-CDW order and its fluctuations. Moreover, Extended Data Fig. 4b shows an image in which the K-CDW switched from that of Extended Data Fig. 4a to that of Extended Data Fig. 4c during the acquisition. This change that occurred during the scan indicates that the K-CDW switches instantaneously on the timescale of the scan speed. This can also indicate either a change of the K-CDW on the entire sample in case of a homogeneous K-CDW, or the displacement of domains with different K-CDW configurations separated by domain walls. It is noted that this concerns only this anomalous K-CDW, which coexists with the KB order, the latter being unchanged in the three images (the bright bonds pattern remains the same).

Such transitions of the K-CDW happened a few times during our measurements. In Extended Data Fig. 5a, we show a 10×10 nm^2 image of an asymmetric KB pattern with the circle-like pattern formed by the merging of the strong bonds inside one hexagon of the KB order unit cell. Imaging the same area a few minutes later in Extended Data Fig. 5b unveils a spontaneous change of K-CDW configuration, similar to that in Extended Data Fig. 4b, which occurred during scanning on the line indicated by the red arrows: in the top part, the three strong bonds merge together inside another hexagon of the KB order unit cell with respect to the bottom part (see the white dashed line that intercepts

the circles in the top part of the image and, conversely, passes between the circles in the bottom part). As previously, the KB order lattice itself does not change.

We point out that we cannot exclude a K-CDW configuration change induced by the action of the scanning tip. Still, such a tip-induced change also implies that the K-CDW is not pinned and can be subject to fluctuations.

Induced t_2 asymmetry in the CDW state

We discuss here how a second-nearest-neighbour hopping asymmetry gaps the zLL of graphene. We consider the spinor $\psi = (\psi_{AK}, \psi_{BK}, \psi_{AK'}, \psi_{BK'})$, where $\psi_{\sigma\tau}$ is a zLL single-particle wavefunction in sublattice σ and valley τ. In this basis, both the sublattice imbalance $\Delta n = n_A - n_B$ and the second-nearest-neighbour hopping asymmetry $\Delta t_2 = t_{2A} - t_{2B}$ (Extended Data Fig. 6) enter the low-energy Hamiltonian close to the Dirac point with the matrix $\tau_0 \otimes \sigma_z$ in valley (τ) and sublattice space (σ). This matrix structure implies that both perturbations gap out the K and K' points of graphene, with a gap given by[30]:

$$E_g = \Delta n + \frac{3}{2}\Delta t_2, \tag{1}$$

which is of equal sign for both valleys. We can visualize the effect of Δt_2 and Δn on the zLL by diagonalizing the graphene Hamiltonian in the presence of a magnetic field. The spectrum with $\Delta t_2 \neq 0$ and $\Delta n \neq 0$ are shown in Extended Data Fig. 6a, b, respectively, obtained with the kwant package[49]. We can confirm numerically that the gap is given by equation (1) and that when $\Delta n = -\frac{3}{2}\Delta t_2$ the gap closes, confirming that both perturbations enter the Hamiltonian with the same matrix structure.

The above argument suggests that interactions that induce a finite Δn will generically induce a finite $\Delta t_2 \neq 0$, as they both enter with the same matrix structure. To exemplify this generic behaviour, we use the Hamiltonian of graphene in the presence of nearest-neighbour interactions V_1:

$$H = -t\sum_{\langle ij \rangle} (c_i^\dagger c_j + \text{h.c.}) + V_1\sum_{\langle ij \rangle} n_i n_j, \tag{2}$$

where the sums are taken over nearest neighbours of the honeycomb lattice. Here $c_i^\dagger$ and c_i are the creation and annihilation operators, respectively, acting on site i of the honeycomb lattice, and h.c. denotes Hermitian conjugate. It is noted in particular that the second-nearest-neighbour hopping is explicitly zero in the Hamiltonian. In the limit of infinitely large interaction, the ground state of H at half-filling is a CDW with one fully occupied and one fully empty sublattice, a state characterized by $\Delta n = 1$. The bond asymmetry Δt_2 is expected to be exactly zero in this limit, as all sites on one sublattice are completely full and thus no states are available to hop to. Similarly, all sites on the other sublattice are completely empty such that no states are available to hop from. At sufficiently large (but finite) V_1/t, the ground state is a CDW with partial sublattice imbalance, as we numerically show in Extended Data Fig. 7. In Extended Data Fig. 7a, we show the expectation value $\Delta n = \langle c_{iA}^\dagger c_{iA} - c_{iB}^\dagger c_{iB} \rangle$, where $c_{i\tau}$ and $c_{i\tau}^\dagger$ act on unit cell i of sublattice τ, in the ground state of H for different V_1 obtained by using the infinite density matrix renormalization group, implemented using the tenpy package[50], as explained in ref. [28]. For small interactions, Δn is close to zero, and grows continuously to one as V_1 is increased[28], signalling a second-order phase transition (see, for example, ref. [28] for a discussion). As shown in Extended Data Fig. 7b, we observe a concomitant second-nearest-neighbour bond asymmetry, defined as $\Delta t_2 = \text{Re}[\langle c_{iA}^\dagger c_{i+1A} - c_{iB}^\dagger c_{i+1B} \rangle]$, that develops at intermediate values of V_1, as expected on the basis of our previous symmetry discussion. As V_1 increases, Δt_2 increases until reaching a maximum, and then decreases as V_1 becomes larger, for all cylinder circumferences $L_y = 6$, $L_y = 8$ and $L_y = 10$. It is possible to check numerically that setting $t = 0$ in

equation (2), that is, in the limit $V_1/t \rightarrow \infty$, leads to $\Delta t_2 = 0$ and $\Delta n = 1$, as discussed above.

The above results support that a CDW order with a partial sublattice imbalance, that is, $0 < \Delta n < 1$, is generically accompanied by a second-nearest-neighbour bond asymmetry, $\Delta t_2 \neq 0$, as argued in the main text.

In the zLL of graphene, the wavefunctions at each valley live in different sublattices and thus a full valley polarization implies a full sublattice polarization $\Delta n = 1$, in which case $\Delta t_2 = 0$. When the sublattice polarization is not maximal then a finite Δn and Δt_2 are expected, consistent with what is observed in experiment (Fig. 5). As mentioned in the main text, this effect can originate from Landau level mixing as the sublattice index is not locked to the valley index beyond the zLL[31–33].

Influence of the moiré superlattice on the CDW phase

The sample AC23 shows a weak moiré superlattice (weak in the sense that is not always visible in our images). This raises the question of whether the CDW phase we observed was induced by the moiré pattern, which could also break the sublattice symmetry, or not. In such case, we may expect the CDW pattern to rely on that of the moiré pattern, with the sublattice polarization depending on the position inside the moiré superlattice (owing to the periodic potential it induces in graphene). Extended Data Fig. 8b shows a CDW phase observed at $B = 7$ T. The moiré pattern is barely visible but appears as bright spots, such as the ones indicated by dashed white circles. The CDW pattern itself is homogeneous over the whole moiré lattice.

STM images of the similar sample AC24 on $SrTiO_3$ did not show any moiré superlattice. Still, in the same conditions, at charge neutrality, we observed signatures of a CDW phase, shown in Extended Data Fig. 9b, which indicates that the CDW we observe in our $hBN/SrTiO_3$ samples is indeed an intrinsic consequence of many-body interactions at charge neutrality and not due to extrinsic substrate-induced sublattice symmetry breaking.

Disappearance of the CDW order at low magnetic field

Extended Data Fig. 8a, b shows that the CDW persists at $B = 9$ T and $B = 7$ T on sample AC23. However, Extended Data Fig. 8c–e at $B = 4$ T does not show the CDW anymore but only the usual sublattice-unpolarized honeycomb lattice.

Finally, it is theoretically expected[10] that graphene undergoes a first-order phase transition from the CDW to the F phase. Such a transition should induce the formation of domains in graphene with the coexistence of both phases around the magnetic field at which the transition occurs. When taking a closer look at Extended Data Fig. 8e taken at $B = 4$ T (see its zoom in Extended Data Fig. 8f), one can discern some bright dots in some parts of the image (see the blue circles). This residual asymmetry of the honeycomb lattice is reminiscent of the CDW. It is possible that it may constitute a signature of such domains around the transition between the CDW and F phases.

Data availability

All data described here are available at Zenodo[51].

42. Wang, L. et al. One-dimensional electrical contact to a two-dimensional material. *Science* **342**, 614–617 (2013).
43. Li, X.-X. et al. Gate-controlled reversible rectifying behaviour in tunnel contacted atomically-thin MoS_2 transistor. *Nat. Commun.* **8**, 970 (2017).
44. Choi, Y. et al. Electronic correlations in twisted bilayer graphene near the magic angle. *Nat. Phys.* **15**, 1174–1180 (2019).
45. Sakudo, T. & Unoki, H. Dielectric properties of $SrTiO_3$ at low temperatures. *Phys. Rev. Lett.* **26**, 851–853 (1971).
46. Hemberger, J., Lunkenheimer, P., Viana, R., Böhmer, R. & Loidl, A. Electric-field-dependent dielectric constant and nonlinear susceptibility in $SrTiO_3$. *Phys. Rev. B* **52**, 13159 (1995).
47. Sachs, R., Lin, Z. & Shi, J. Ferroelectric-like $SrTiO_3$ surface dipoles probed by graphene. *Sci. Rep.* **4**, 3657 (2014).
48. Chen, S., Chen, X., Duijnstee, E. A., Sanyal, B. & Banerjee, T. Unveiling temperature-induced structural domains and movement of oxygen vacancies in $SrTiO_3$ with graphene. *ACS Appl. Mater. Interfaces* **12**, 52915–52921 (2020).
49. Groth, C. W., Wimmer, M., Akhmerov, A. R. & Waintal, X. Kwant: a software package for quantum transport. *New J. Phys.* **16**, 063065 (2014).
50. Hauschild, J. & Pollmann, F. Efficient numerical simulations with tensor networks: Tensor Network Python (TeNPy). SciPost Phys. Lect. Notes 5, https://doi.org/10.21468/SciPostPhysLectNotes.5 (2018).
51. Coissard, A. et al. Data for Imaging tunable quantum Hall broken-symmetry orders in graphene. Zenodo https://doi.org/10.5281/zenodo.5838139 (2022).

Author contributions A.C. and H.V. fabricated the samples. A.C. and D.W. performed the measurements. A.C., D.W., H.S. and B.S. analysed the data. A.G.G. and C.R. conducted the theoretical analysis. K.W. and T.T. supplied the hBN crystals. F.G. provided technical support on the experiment. C.W. and H.C. contributed to the discussion. B.S. conceived the project and wrote the paper with inputs from all co-authors.
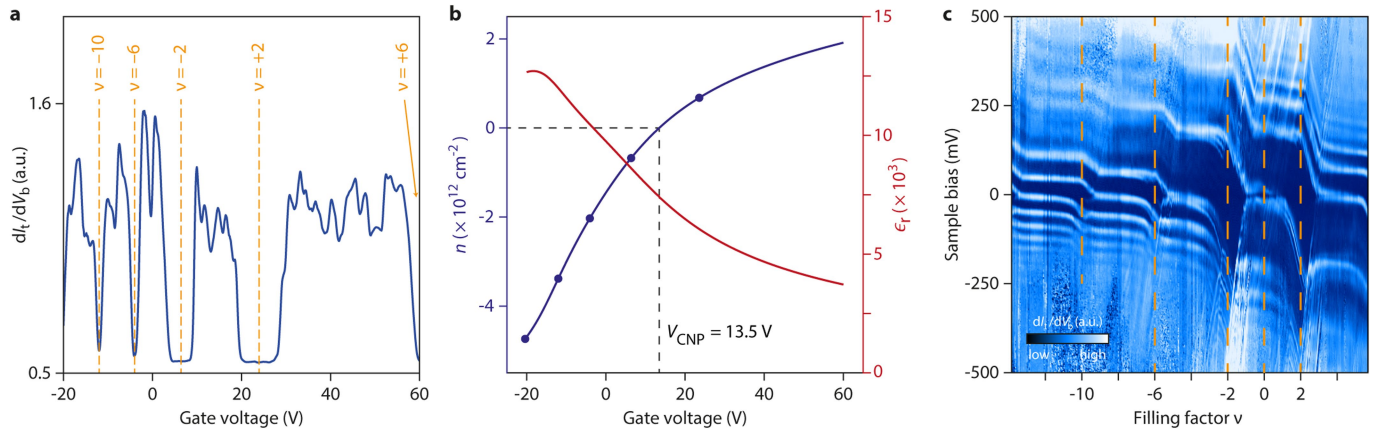
**Extended Data Fig. 1 | Estimation of the dielectric constant of SrTiO₃ and rescaling of the gate map. a**, Line cut at $V_b = 0$ V, averaged on a range of ±20 mV, of the dI_t/dV_b gate map in Fig. 2a. **b**, Estimation from the filling factors obtained in **a** of the charge carrier density n (blue dots), its polynomial fit (blue curve), and computed values of $\epsilon_r \simeq \epsilon_{STO}$ (red curve), as a function of gate voltage. The fit yields $V^{CNP} \simeq 13.5$ V. **c**, Rescaling of the gate map of Fig. 2a as a function of v.
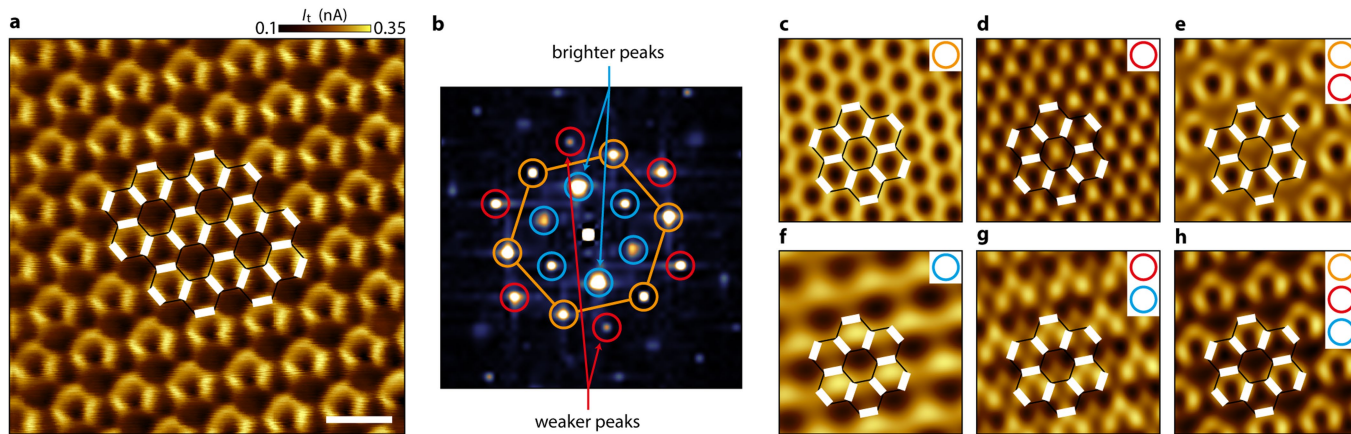
Extended Data Fig. 2 | 2D-FT decomposition of the asymmetric Kekulé distortion. a, 3×3 nm² image showing an asymmetric KB pattern, measured at $B = 14$ T and $V_b = 2$ mV. **b**, 2D Fourier transform (2D-FT) of the STM image in **a**. Yellow circles indicate peaks of the honeycomb lattice, red and blue circles indicate peaks of the bond-density wave. **c**–**h**, 1.53×3 nm² Filtered images obtained by considering certain peaks of the FFT as indicated in the top right corner of each panel. The Kekulé lattice is drawn in white for reference. The KB order is mostly retrieved by considering only the yellow and red peaks. The asymmetry of the KB pattern is encoded in the blue peaks whose two of them are twice as high as the others due to the K-CDW order. Scale bar is 500 pm.
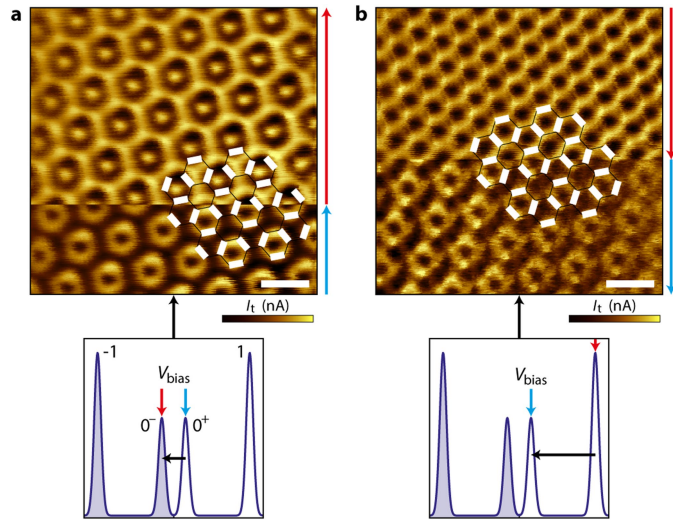
Extended Data Fig. 3 | Contrast inversion and emergence of the Kekulé bond order. $3 \times 3 \, nm^2$ STM images during which we changed the bias voltage as shown in the bottom insets (the current color bars are tuned separately for each half of the images). **a**, We start (bottom) at $V_b = 32 \, mV$ (LL_{0+}) and switch (top) to $V_b = -12 \, mV$ (LL_{0-}) to observe a contrast inversion of the KB lattice. **b**, We start (top) at $V_b = 200 \, mV$ (LL_1) and switch (bottom) to $V_b = 20 \, mV$ (LL_{0+}) and observe the emergence of the KB order from the honeycomb lattice. Scale bars for both images are 500 pm.
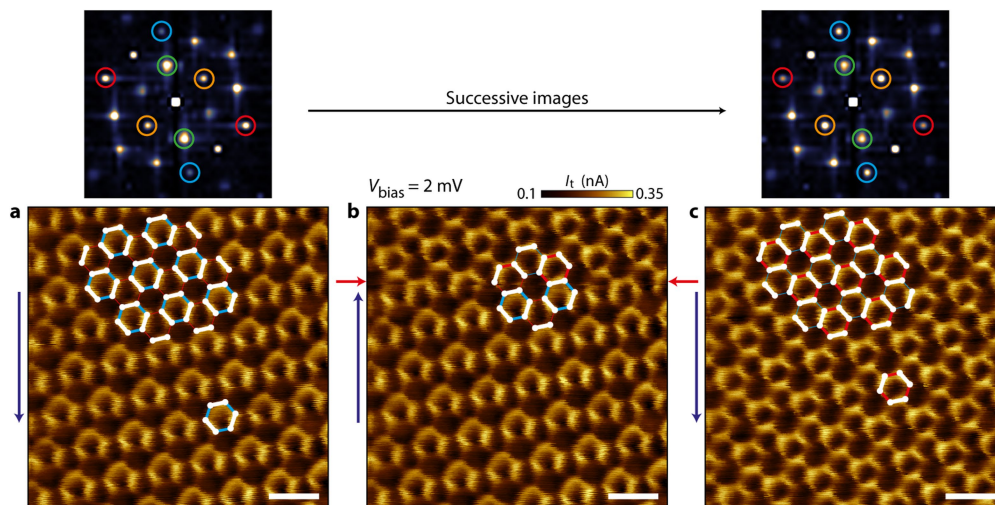
Extended Data Fig. 4 | Asymmetry reversal of the Kekulé pattern. 3×3 nm^2 STM images measured at $B = 14$ T, $V_b = 2$ mV and at the same position. The three images were measured successively (scanning time : 1 min). A jump occurs in **b** at the scan line indicated by the red arrows, leading to an inversion of the asymmetry of the Kekulé pattern. The slow scan axis direction is indicated by the blue arrows on the left of each image. Scale bars for the three images are 500 pm.

a

b

$V_{bias} = 25$ mV

I_t (nA)

0 ▬▬ max

$V_{bias} = 25$ mV
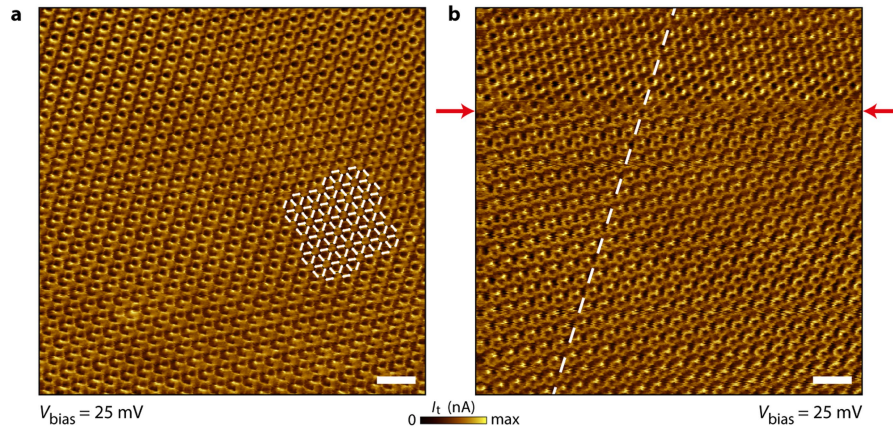
Extended Data Fig. 5 | Change of the Kekulé asymmetry. 10×10 nm^2 STM images measured at $B = 14$ T and $V_b = 25$ mV. In **b**, the asymmetry pattern changes at the scan line indicated by the red arrows. Scale bars for both images are 1 nm.
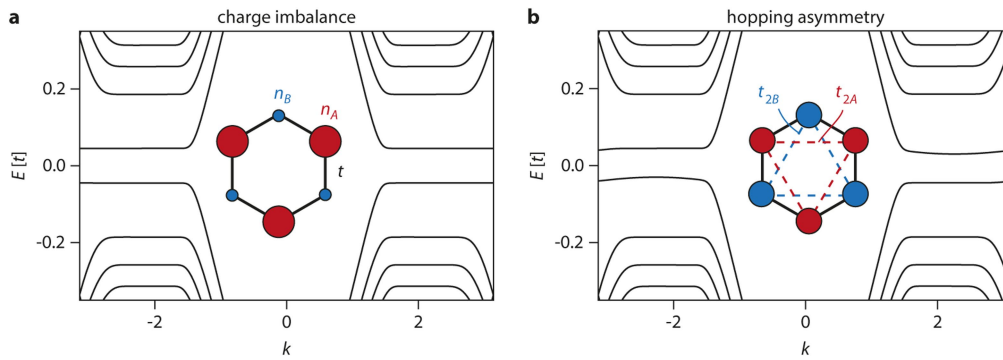
Extended Data Fig. 6 | Effect of sublattice charge imbalance and a t_2 asymmetry on the zeroth Landau level. a shows that the effect of a finite charge imbalance $\Delta n = n_A - n_B$ is to gap the zeroth Landau level of graphene. **b** shows that a hoping asymmetry $\Delta t_2 = t_{2,A} - t_{2,B}$ also opens up a gap, that depends on momentum k as we move away from the K and K' points. The parameters are chosen so that E_g is the same on both plots at the K and K' points, according to Equation (1). Simulations were performed using the kwant software[49] for a 41×41 hexagonal lattice with $\phi = 0.003$ flux per plaquette, in units of the flux quantum. Energies are measured in units of the nearest-neighbor hopping t. For **a**, $\Delta t_2 = 0$ and $\Delta n = 0.045$, while for **b**, $\Delta t_2 = 0.015$ and $\Delta n = 0$.
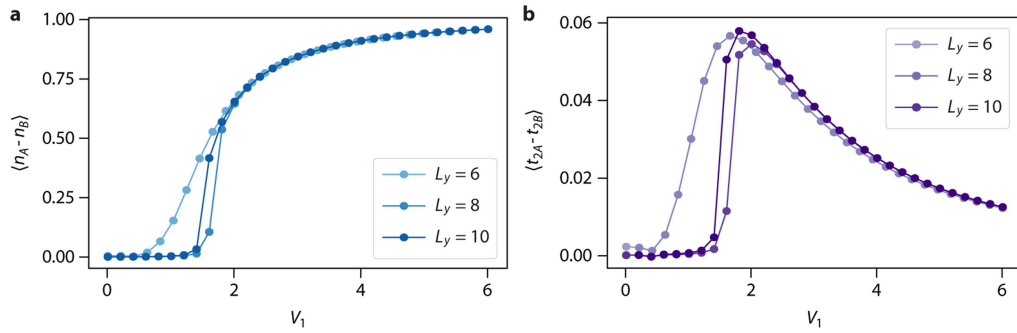
Extended Data Fig. 7 | Induced Δt_2 asymmetry by interactions. a shows that a sublattice charge imbalance $\Delta n = \langle n_A - n_B \rangle \neq 0$ develops as V_1 increases. **b** shows the concomitant emergence of a second nearest-neighbor bond asymmetry $\Delta t_2 = \langle t_{2A} - t_{2B} \rangle \neq 0$, peaking at intermediate values of V_1. The simulations are carried out for cylinder circumferences of $L_y = 6, 8, 10$ sites, all with bond-dimension $\chi = 1000$, using the tenpy package[50].
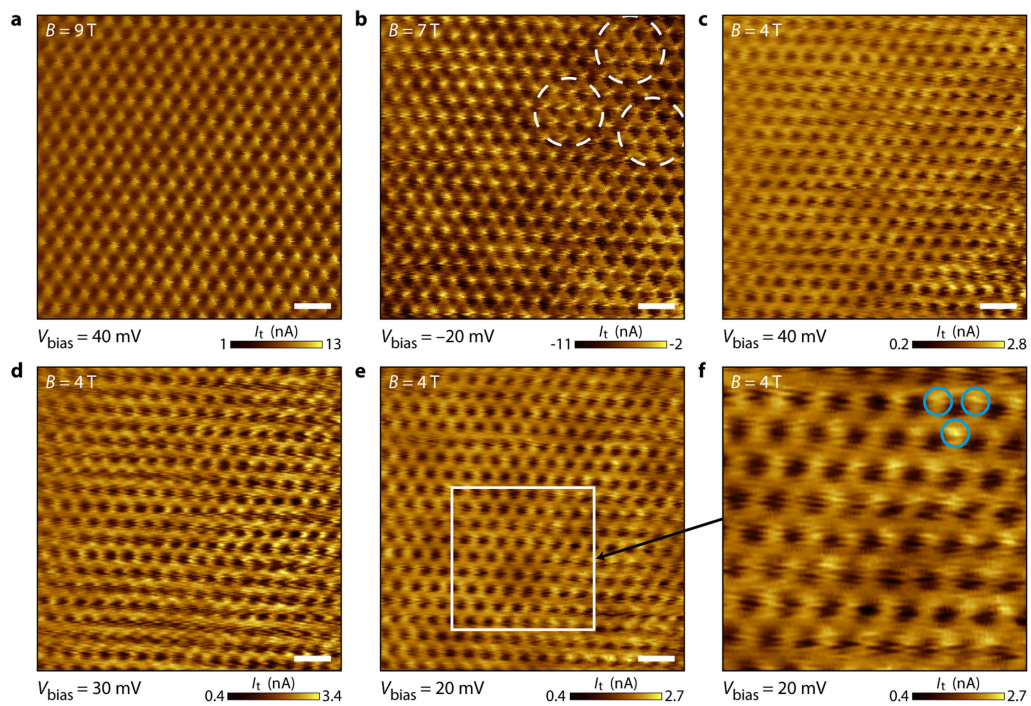
Extended Data Fig. 8 | Disappearance of the charge-density wave at low magnetic field in sample AC23. a, CDW at $B = 9$ T. **b**, CDW at $B = 7$ T. The Moiré superlattice is visible but does not perturb the CDW pattern. **c**, **d**, Honeycomb lattice with no CDW at $B = 4$ T. **e**, Honeycomb lattice at $B = 4$ T with residual traces of CDW, see the zoom in **f** of the white rectangle. Scale bars for all figures are 500 pm.

$V_{bias} = -350$ mV   0 ▬▬ Z (pm) 25 $V_{bias} = -18$ mV   0 ▬▬ Z (pm) 25
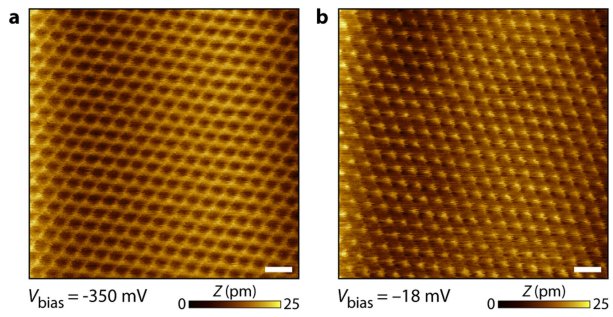
Extended Data Fig. 9 | Charge-density-wave order in sample AC24.
a, Honeycomb lattice at $B = 14$ T and $V_b = -350$ mV observed at $v = 0$. **b**, CDW under the same conditions but at $V_b = -18$ mV. Scale bars for both figures are 500 pm.

Extended Data Table 1 | Geometrical parameters of the four measured samples

Sample	AC04	STO07	AC23	AC24
Substrate	Si^{++}/SiO_2	$SrTiO_3$	$SrTiO_3$	$SrTiO_3$
Substrate/oxide thickness	285 nm	500 μm	500 μm	500 μm
hBN thickness (d_{BN})	14 nm	8 nm	12 nm	10 nm